Structurally distinct oligomers of islet amyloid polypeptide mediate toxic and non-toxic membrane poration

Melissa Birol,[1,2] Sunil Kumar,[3] Elizabeth Rhoades,[2,*] and Andrew D. Miranker[1,*]

1 Department of Molecular Biophysics and Biochemistry, Yale University, 260 Whitney Avenue, New Haven, CT 06520
2 Department of Chemistry, University of Pennsylvania, 231 South 34th Street, Philadelphia, PA 19104
3 Department of Chemistry, New York University, Silver Center for Arts and Science, 100 Washington Square East, 10th Floor, New York, NY 10003

* Correspondence: andrew.miranker@yale.edu, elizabeth.rhoades@sas.upenn.edu
Lead Contact: Andrew Miranker

Manuscript Type: New Results
Running Title: IAPP forms toxic and non-toxic membrane pores
Keywords: giant plasma membrane vesicle, small molecule, toxic oligomer, amylin

Summary

Peptide mediated gain-of-toxic function is central to pathology in diseases such as Alzheimer's and diabetes. Cytotoxicity has long been correlated with self-assembly of the peptides into membrane-associated oligomers. The relationship of such species to membrane poration and the nature of poration's effects on toxicity remain elusive. Here, we focus on islet amyloid polypeptide (IAPP), a hormone associated with β-cell loss in diabetics. Newly developed membrane leakage and diluted-FRET methods enable structure-function inquiry to focus on large *N*, homooligomers. Our results not only show the coexistence of two mechanisms of poration, but reveal that only one is cytotoxic. At no point do the porating conformations of IAPP match those of aqueous prepared amyloid. Membrane associated oligomers are internally dynamic and grow in discrete steps consistent with liquid-like fusion. Toxic permeation can be localized to mitochondria using a structure specific-ligand, illuminating a strategy for small molecule development applicable to partially ordered proteins.

Highlights

- The peptide amyloid precursor, IAPP, forms two classes of membrane porating oligomers.
- The two classes have a >100-fold difference in pore size with the large pore form correlated with mitochondrial depolarization and toxicity.
- A drug-like molecule distinguishes between the two oligomer classes and rescues toxicity by stabilizing non-toxic poration without displacing IAPP from the mitochondria.
- The mechanism of oligomer assembly is consistent with a stepwise coalescence of liquid-like droplets.

Introduction

Achieving molecular scale insights in structure-function faces unique challenges when function arises from oligomers formed from partially ordered proteins. Attention to proteins in this class has dramatically increased in recent years as such systems leverage liquid-liquid phase separation to affect transient self-assembly of dynamic structures (Courchaine et al., 2016). This can occur in aqueous and membrane milieus, for example, giving rise to nucleoli (Brangwynne et al., 2011) and signaling complexes (Su et al., 2016) respectively. As is often the case in biology, functional examples are a consequence of evolution leveraging an intrinsic physical property of polypeptides. Unchecked, however, this property can also result in the pathological assembly of normally benign peptides into entities whose gains-of-function include cytotoxicity (Aguzzi and Altmeyer, 2016).

The spontaneous assembly of proteins underpins numerous important human diseases including Alzheimer's, Parkinson's and type II diabetes (Knowles et al., 2014). In each case, a different protein and *in vivo* milieu is involved, however the broad characteristics include formation of pre-amyloid assemblies from which toxic gains-of-function are predominantly believed to emerge. These pre-amyloid toxins can occur spontaneously in solution, or by encounter with a biological polyanion such as a phospholipid bilayer or, as has recently been suggested, polyphosphate (Cremers et al., 2016). An additional origin of toxicity is catalysis mediated by the lateral walls of performed amyloid (Knowles et al., 2014; Schlamadinger and Miranker, 2014). This latter phenomenon may reconcile conflicting opinions regarding the amyloid versus pre-amyloid origin of cytotoxicity since the rate of formation of pre-amyloid toxins can be dependent on amyloid.

Islet amyloid polypeptide (IAPP) is a 37-residue peptide-hormone copackaged and cosecreted with insulin by the endocrine pancreas. In type II diabetics, this peptide is observed to form amyloid fibers that are associated with loss of β-cell mass (Mukherjee A, 2015). Sequence variants of IAPP from species that do not spontaneously develop diabetes, such as rodents, show a low propensity to form amyloid. Correspondingly, mutational analyses reveal a strong correlation between amyloid formation potential and cytotoxicity. However, it is the process of amyloid formation and not the fibers themselves that are toxic. This suggests amyloid is but one consequence of the formation of pre-amyloid oligomeric assemblies (Brender et al., 2008). In solution, IAPP weakly samples α-helical conformations that are

stabilized upon interaction with phospholipid bilayers. Pre-amyloid structures include lateral self-association into helical oligomers that include parallel and anti-parallel topologies (Nath et al., 2011). The functions arising from assembly include energy independent membrane translocation, membrane poration and mitochondrial localization (Costes et al., 2013b). At the molecular level, the relationships of structures to functions, including downstream observations of mitochondrial dysfunction and cell death, remain unclear.

Membrane interacting oligomers whose structures and dynamics result in poration are widely believed to underpin IAPP's toxic gain-of-function (Mukherjee et al., 2015). IAPP may self-assemble and porate intracellularly or extracellularly; a distinction that may be moot given that IAPP has energy independent membrane penetrating qualities (Magzoub and Miranker, 2012). As IAPP localizes to mitochondria in cultured cells in a manner correlated with cell death, it is an appealing, but unproven idea that IAPP directly mediates poration of mitochondria and that this is the origin of β-cell dysfunction (Kegulian et al., 2015). Consider, for example, that poration of mitochondria has been shown instead to increase the viability of β-cells and rescue metabolic syndrome in animal models (Perry et al., 2015). How does one reconcile these conflicting observations? Clearly a deeper insight is required to understand the molecular basis of IAPP mediated poration and its relationship to toxicity.

To address this challenge, we first developed a structure-based fluorescence approach, referred to as diluted-FRET, which brings the focus of data gathering onto large, homooligomeric assemblies. Taking this tool into live cells enables structural characterization; however, time dependent changes to intracellular oligomers vary in rate and time of initiation of the oligomerization pathway. In contrast, synchronous initiation of protein self-assembly and associated gains-of-function, such as permeation, are possible on model membrane bilayers. To credibly synergize studies conducted in these two milieus, we have engineered a kinetic leakage assay that uses a minimally processed, cell-derived membrane. Importantly, we are able to couple live-cell to cell-derived bilayer observables through the use of a structure-specific small-molecule binder of intracellular IAPP.

Results

Leakage profiles using a cell derived membrane

IAPP induces leakage in giant plasma membrane vesicles (GPMVs) in a protein concentration-dependent manner. GPMVs were prepared from live INS-1 cells as previously described (Schlamadinger and Miranker, 2014; Sezgin et al., 2012) with an additional step of pre-staining the cytoplasm using a thiol-reactive fluorescent probe, CellTracker Orange. These GPMVs are stable for days with little loss of fluorescence even under prolonged confocal imaging (Figure 1A). Membrane leakage kinetics of 5 μM GPMVs (expressed as apparent concentration in phospholipid monomer units) were monitored as a loss in fluorescence intensity after co-addition of IAPP and 1 mM of the small molecule fluorescent quencher, acid-blue 9 (AB9) (Figure 1D). At 2:1, 5:1 and 10:1, protein:lipid (P:L), single exponential decay is observed, ending in complete loss of fluorescence (Figure 1D). Rate constants are relatively insensitive to protein concentration, with $42 \pm 6\ s^{-1}$, $54 \pm 5\ s^{-1}$ and $60 \pm 3\ s^{-1}$ observed for 2:1, 5:1, and 10:1 P:L, respectively. High P:L ratios such as those used here are associated with destruction of synthetic lipid vesicles (Kegulian et al., 2015). However, these P:L are consistent with standard application of amyloid precursors to cell culture where the addition of low μM protein to a culture plate corresponds to P:Ls of 100:1 or more. This routine, 5+ order of magnitude disparity, has been noted as a potential cause for concern when interpreting solution biophysical results (Wimley, 2010). That we observe no gross changes to the GPMV morphology at these P:L suggests that our model membrane retains the robustness of the plasma membrane, possibly a consequence of the retention of cytoskeletal components (Podkalicka et al., 2015).

Leakage profiles monitored using luminal loss as an alternative reporter are characterized by two kinetic decays separated by a lag time. Membrane permeation was assessed as above, but without the use of an added quenching agent. In this case the leakage kinetics reflect the exit of fluorescently labeled cytoplasmic components from the GPMVs, rather than the diffusion of the small molecule quencher into the GPMV lumen. Remarkably, two kinetic phases of leakage are observed (Figure 1B and 1E). At 10:1, P:L, the first phase fits to a single exponential decay with a rate constant of $33 \pm 2\ s^{-1}$ reaching a plateau in which 48 ± 4% of the starting fluorescence is lost. A second decay begins after a lag of 1400 ± 200 s. This second kinetic phase also fits to a single exponential decay with a rate constant $49 \pm 2\ s^{-1}$. At 5:1,

the rate constants for leakage are slightly diminished while the lag-phase is more noticeably affected (Figure 1E). At the lowest stoichiometry assayed, 2:1, only the first leakage phase is evident on the timescale of observation (Figure 1E). Plainly the lag period is strongly sensitive to protein concentration while the rate constants are not. This suggests that while two IAPP mediated changes to the GPMVs occur, the resultant leakage kinetics are not strongly rate limited by the protein concentration.

IAPP forms two classes of pore distinguishable by size. In the above assays, performed in the absence of quencher, changes in intensity reflect the loss of labeled molecules from the lumen. As cytoplasmic components are variable in size, we used fluorescence correlation spectroscopy (FCS) to assess the diffusion of molecules that have leaked to the surrounding buffer. During the first of the two kinetic phases of leakage, no large particles are observed (Figure 1H). Correlation analysis is possible and fits are readily made to an analytical form that includes only a single diffusing species. This gives a diffusion constant of 390 ± 25 $\mu m^2/s$. Using the Stokes-Einstein approximation, this corresponds to an average molecular weight of ~700 Da. In marked contrast, data collection during the second phase of leakage is characterized by large irregular bursts (Figure 1H). This reflects the presence of much larger and heterogeneous species (Elbaum-Garfinkle et al., 2010). Experimental limitations prevent rigorous characterization but particles larger than ~200 kDa is a reasonable estimate. Clearly, the two phases of leakage are characterized by a transition from one in which only small consistently sized holes are present to one in which large heterogeneous defects are formed.

The assemblies of IAPP that give rise to alternative leakage profiles are structurally distinct. Recently we reported the development of a tetraquinoline amide, ADM-116. This molecule demonstrates cytotoxic rescue through specific binding interactions with α-helical states of membrane bound IAPP (Kumar et al., 2016a; Kumar et al., 2016b). Moreover, ADM-116 can cross plasma membranes and act on intracellular IAPP making it ideally suited for making matched assessments inside cells (see below). Leakage profiles were collected on GPMVs at a P:L of 10:1 and with the addition of ADM-116 equimolar with IAPP (Figure 1C and 1F). The resultant profiles fit to single exponential decay with a rate constant of 34 ± 1 s^{-1} and an amplitude of 52 ± 3 %. FCS measurements of the media show no evidence of release of large heterogeneous species (Figure 1H). Correlation analysis of leaked materials under these conditions yields a diffusion constant of 480 ± 50 $\mu m^2/s$, closely similar

to that of materials leaked in the absence of ADM-116 during the first phase. Most significantly, ADM-116 has no effect on the first leakage process and appears to wholly inhibit the second.

The presence of two classes of pore is a property of IAPP, and not intrinsic to the GPMV based assay. First, we consider the mitochondrial uncoupling reagent, 2,4-dinitrophenol (DNP), which was recently reformulated to rescue cytotoxicity in animal models of diabetes (Perry et al., 2015). A concentration of 10 μM DNP induces GPMVs to leak at a rate of $58 \pm 8\ s^{-1}$ (Figure 1G). This loss of intensity plateaus with ~50% of fluorescence remaining. By FCS, no large particles emerge from the GPMVs upon leakage (Figure S1). Correlation analysis is readily accommodated by fits to single species giving a diffusion constant, $420 \pm 24\ \mu m^2/s$, within error of that observed using IAPP. Importantly, inducing leakage using this small molecule does not reveal a two-phase process and indeed more closely resembles leakage induced by IAPP when in complex with ADM-116. Second, the sequence variant of IAPP from rat is routinely used as a control peptide as it is not amyloidogenic and requires highly elevated concentrations to display even weak cytotoxicity (Magzoub and Miranker, 2012). At 200 μM (P:L=40:1), rat IAPP leakage is observable on the same timescale as human IAPP (Figure 1G). Some additional leakage is apparent, plateauing after a day, but total loss of intensity is ~50%, with no further changes detected even after 4 days (Figure 1G). The contrasting behavior of human IAPP with DNP and rat IAPP clearly shows that the two phases of human IAPP induced leakage are specific to this variant of the peptide.

Intracellular loss of membrane integrity

IAPP localization to mitochondria is correlated with depolarization. IAPP induced toxicity in cells has been associated with several cellular membranes, most notably mitochondria. This is observed under conditions where IAPP is expressed (Gurlo et al., 2010) or introduced exogenously into the culture medium (Kumar et al., 2016b; Magzoub and Miranker, 2012). Mitochondrial uncoupling in response to IAPP has been previously reported (Soty M, 2011), but without assessment of correlation with IAPP localization. Here, we have used the membrane potential sensitive dye, JC-1, to monitor mitochondrial polarization in live INS-1 cells (Figure 2A). Addition of 13 μM IAPP to the culture media results in greater than 50% cell death after 48 h (Figure S2). Imaging performed at 24 h shows widespread mitochondrial localization accompanied by loss of polarization (Figure 2B and 2E).

Overlap analysis across 50 cells shows ~60% of observable IAPP to be associated with depolarized mitochondria (Figure 2F). By 48 h the extent of loss in membrane polarization is quadrupled (Figure 2B and 2E). At 5 μM IAPP, INS-1 cells experience a reduced cytotoxicity of ~15% at 48 h (Figure S2). Mitochondrial depolarization at 24 h and at 48 h is still evident (Figure 2C and 2E) but greatly diminished relative to the more toxic condition. IAPP colocalization to depolarized mitochondria is still evident albeit reduced to ~20% of the total IAPP (Figure 2F). In contrast, IAPP overlap with ER is 5% and 7% for these two conditions respectively (Figure 2H, 2I and 2J). Thus, localization of IAPP to mitochondria appears to be strongly associated with depolarization. Moreover, it is the extent of depolarization that distinguishes the strongly versus weakly toxic condition.

Cytotoxic rescue by ADM-116 significantly diminishes the correlation of IAPP with mitochondrial depolarization. Under our standardized rescue condition, 13 μM ADM-116 added to culture media 3 h after uptake of 13 μM IAPP, depolarization at 24 h is markedly reduced (Figure 2D and 2E) as is the overall apparent extent of IAPP association with depolarized mitochondria (Figure 2F). The capacity of ADM-116 to reduce mitochondrial depolarization remains potent through 48 h incubation (Figure 2E). Importantly, rescue of IAPP induced toxicity with ADM-116 does not significantly change the overall amount of protein localized with mitochondria (Figure 2H), nor the fraction of mitochondria with associated IAPP (Figure 2G). Moreover, neither rescue with ADM-116 nor a reduction in toxicity using less IAPP wholly eliminates depolarization (Figure 2E). For comparison, experiments were performed in which mitochondria were manipulated instead by incubating with DNP. At routinely used concentrations (5 μM and 10 μM), we find DNP is weakly toxic and JC-1 measured mitochondrial polarization is unaffected (Figure S3). This is analogous to reports using yeast that show that sub-toxic levels of DNP induce changes in mitochondrial respiration without significant loss of membrane polarization (Antonenko et al., 2013). It is therefore plausible that small pore leakage induced by IAPP in the presence of ADM-116 is not sufficient to cause depolarization of cellular mitochondria.

Coarse grain structural analysis via intermolecular FRET

Structural analysis of IAPP oligomers was performed via intermolecular FRET. Briefly, single labeled IAPPs are prepared in which either a donor (Alexa 488, $IAPP_{A488}$) or acceptor (Atto 647, $IAPP_{A647}$) fluorophore is covalently attached to the N-terminus of IAPP. We deviate from typical intermolecular FRET protocols by performing experiments under conditions where labeled IAPP is mixed with a high proportion of unlabeled IAPP. This approach, which we term "diluted-FRET", draws observation to the subset of IAPP oligomers that are sufficiently large to harbor at least one donor and acceptor pair under the diluted condition.

Intracellular IAPP oligomers form a distinct species when inhibited by a structure specific small molecule binder. INS-1 cells were incubated with 10 μM IAPP doped with 0.1 μM each of $IAPP_{A488}$ and $IAPP_{A647}$. The small molecule ADM-116 was added to culture media after 3 h to ensure most of the IAPP was taken up by the cells (Kumar et al., 2016b). Imaging conducted at 24 h (Figure 3A) shows intracellular, intermolecular FRET to be widespread. The FRET efficiency ($FRET_{eff}$) histograms of individual cells are directly comparable to averages conducted over many cells (Figure 3B) and show a single, very narrow and time invariant distribution with a peak efficiency of 0.60 ± 0.07. After 48 h, a minor change in distribution reaches a $FRET_{eff}$ of 0.61 ± 0.06. A narrow distribution is wholly unexpected as under conditions of diluted-FRET, numerous combinatorial locations for inclusion of donor and acceptors should give a range of $FRET_{eff}$. Analysis using a different FRET pair, $IAPP_{A488}$ and $IAPP_{A594}$, give similar results (Figure S4A). This suggests the fluorophores do not contribute significantly to the structures giving rise to the observation. Plainly, a single, long-lived discrete assembly of intracellular IAPP is formed upon cytotoxic rescue by ADM-116.

Oligomers of IAPP evolve to more compact states under conditions that are cytotoxic. Diluted-FRET was measured using cytotoxic levels of IAPP (10 μM) at 24 h and 48 h. Cumulative analysis of cell images taken at 24 h reveal a broad range of $FRET_{eff}$ dominated by values much greater than 0.5 (Figure 3C). Individual cells as well as small sub-cellular regions of interest (ROIs) (Figure 3D) show recurring and relatively narrow distributions at a small number of reproducible values of $FRET_{eff}$. This suggests the breadth of the cumulative distribution (Figure 3C) to be a consequence of summing contributions from discrete rather than a continuum of species. After 48 h, cells show significant

morphological signs of dysfunction. This is accompanied by FRET distributions shifting to markedly higher efficiencies (Figure 3C and 3D). Analysis using a different FRET pair, $IAPP_{A488}$ and $IAPP_{A594}$, gives comparable results (Figure S4B). Evidently, upon toxic insult with IAPP, intracellular oligomers are formed in which a progressive change in density, size and/or shape results in increasing $FRET_{eff}$.

GPMV associated IAPP:ADM-116 forms species comparable to those observed in intracellular studies. GPMVs were prepared as for leakage studies above, but without the labeling of lumen thiols. Under conditions matched to those that inhibit the second porated state (Figure 1F), FRET is readily apparent with small membrane localized puncta at 2' that behave as foci from which amorphous assemblies evolve at later time points (Figure 4). IAPP does not appear to form a uniform distribution on the membrane as has been observed on GUVs (Gao and Winter, 2015; Kegulian et al., 2015; Seeliger et al., 2012). Using a toroidal ROI that is predominantly occupied by membrane, time dependent changes to $FRET_{eff}$ are apparent and discontinuous, suggestive of discrete transitions (Figure 4C). Starting at the 2' timepoint, at least one intermediate species is sampled before the distribution reaches a $FRET_{eff}$ of 0.47 ± 0.03 which is then maintained for a period of ~20 minutes. A progression to higher $FRET_{eff}$ then continues, reaching a stable position after t=40' with $FRET_{eff}$ of 0.62 ± 0.03. As an alternative to using a small molecule to eliminate the second porated state, IAPP was instead applied at one fifth the concentration (10 μM) (Figure 1E). At this ratio (5:1) of IAPP to lipid, summation of FRET occurring at the membrane reveals that upon equilibration, a single species dominates with an observed $FRET_{eff}$ of 0.63 ± 0.03 (Figure 4D). The overall time-scale to equilibrium and the end-state $FRET_{eff}$ are the same for the two conditions. Thus, under two sets of conditions in which only the first poration state is observed, the progression of change to oligomeric IAPP resembles that observed (Figure 3) in live cells.

Time resolved analysis of diluted-FRET of IAPP, under conditions resulting in complete leakage of GPMVs, indicates the presence of six species (Figure 4E). At protein to lipid ratios of 10:1, the first oligomers appear within the deadtime (< 2 min) of measurement. Over the timescale associated with observation of leakage, five additional assemblies emerge, each with a discrete, approximately Gaussian distribution of $FRET_{eff}$. No specie appears without another disappearing. This suggests that species form in succession, with each one showing greater $FRET_{eff}$ than its predecessor. Comparable changes are observed, albeit with different average FRET values, for an alternate donor/acceptor pair (Figure S4C).

The invariance with choice of fluorophores, and the coincidence of the timescale with that observed for leakage (where IAPP is unlabeled) both suggest that the fluorophore does not contribute significantly to the structures sampled by IAPP. Plainly, the conformational landscape of membrane associated IAPP contains multiple transitions that occur on timescales associated with membrane integrity loss.

The two classes of pores formed by IAPP on GPMVs correspond to distinct species of oligomer distinguishable by their diluted-$FRET_{eff}$. Combining repeats of the above data across multiple GPMVs and across time results in robust characterization of individual species (Figure 5). Under our standard condition for observing two state leakage (IAPP:lipid=10:1), averages over the first 34' reveals diluted-FRET distributions with assemblies showing apparent FRET at 0.21 ± 0.07, 0.36 ± 0.04, 0.41 ± 0.08 and 0.58 ± 0.02 respectively (Figure 5A*i,* 5A*ii* and 5A*iii*). We observe the first three $FRET_{eff}$ peaks to dominate over a period of time in which only small molecule leakage is observed (Figure 1E, H). Analysis between 36' and 46', i.e. the time period over which large molecule leakage initiates, continues to be dominated by ensembles that were previously present (Figure 5A*iv*). Summation across 48' to 60' show a marked shift to two high $FRET_{eff}$ ensembles at 0.78 ± 0.04 and 0.87 ± 0.01 (Figure 5A*v*) with the former dominant over the bulk of this leakage phase (Figure 4F). Under conditions in which the second porous phase is eliminated, i.e. in the presence of ADM-116 (Figure 5B) or at reduced concentrations of protein (Figure 5C), the final $FRET_{eff}$ distributions are each dominated by a peak whose position superimposes with that of the fourth peak observed at the elevated protein concentrations described above. In other words, solution conditions that affect large but not small hole poration (Figure 1), exclusively affect access to two of the six species that are apparent using diluted-FRET.

The two highest $FRET_{eff}$ species observed on GPMVs do not correspond to canonical IAPP fibril structures. In the above analysis (Figure 4B), oligomeric structures are first evident at 2-4 minutes and enlarge throughout the observation time. Determinations of $FRET_{eff}$ using ROIs that encompass IAPP assemblies near but not on a GPMV surface (Figure 6A) give a distribution wholly consistent with the sum of all GPMV surface associated IAPP (Figure 5A*v*). In marked contrast, the $FRET_{eff}$ distribution of fiber controls are broad and possess a single peak with a $FRET_{eff}$ that is greater than what is observed on GPMVs (Figure 6A). It is the Poisson-like distribution of this control that most clearly distinguishes it from leakage competent IAPP oligomers. In addition, IAPP oligomers on and near GPMVs do not

enhance the fluorescence of the amyloid indicator dye, Thioflavin T (LeVine, 1993) (Figure 6B). Systematic error can arise as GPMVs independently contribute to the fluorescence intensity of ThT, and intensity changes in ThT can also result from changes in aggregate size. To accommodate this, an internal control, $IAPP_{A647,}$ was included so that ThT intensity could be renormalized on a pixel by pixel basis. The renormalized response of GPMV generated IAPP aggregates are 6-fold lower than that observed for the aqueous fiber control (Figure 6D). Therefore, the oligomer structures of IAPP associated with membrane leakage cannot be predominantly formed from canonical amyloid fibers. Clearly, toxic and leakage inducing oligomers of IAPP are less compact and considerably more dynamic than amyloid fibers of IAPP.

Discussion

The task of ascribing IAPP structure to function and mechanism faces unusual challenges as its structure is plastic, its oligomeric size is heterogeneous and it undergoes exchange between aqueous and membrane milieus. It is on this background that we interpret our data derived from three tools: IAPP mediated leakage, diluted intermolecular FRET and structure-specific ligand binding.

Two forms of membrane permeation can be mediated by IAPP. This is apparent from two kinetic phases (Figure 1E) and the presence of a discrete change in the pore size from one kinetic phase to the other (Figure 1H). Small molecule binding rescues cells from mitochondrial depolarization (Figure 2) which either directly or indirectly rescues cells from toxicity. This occurs without displacing IAPP from mitochondria (Figure 2G) and by stabilizing an intermediate oligomeric state (Figure 3A and 3B). Qualitatively, this behavior is also apparent on GPMVs (Figure 5B), a milieu where we can additionally determine that second-, but not first-phase leakage is inhibited (Figure 1F). To our knowledge, this is the first direct detection of two phases of membrane leakage mediated by IAPP. Note, dead-time events preceding a measurable kinetic phase using synthetic lipid systems can be seen in published data (Knight et al., 2006);(Kegulian et al., 2015). While these might correspond to a second and very rapid kinetic phase, they are typically and appropriately ignored as they are more apt to be artifacts, for example from mixing or osmotic imbalance. Here, the two reported kinetic phases are comparable in overall time-scale and no dead-time events are apparent. The use of GPMVs was critical to this discovery as GPMVs are mechanically robust compared to large and giant unilamellar vesicle models. This cell-derived membrane model enables us to suggest that nucleated conversion of small pore permeable states to large pore permeation is the origin of gains in toxic function by IAPP. The latter may occur by direct interaction at the mitochondria. Alternatively, toxicity is one of several possible downstream consequences, such as oxidative stress, that can result from such poration (Costes et al., 2013a).

Small pore permeation of membranes by IAPP is mediated by oligomers composed of scores to hundreds of peptides. Most of the $FRET_{eff}$ distributions observed here display peaks whose narrow widths are akin to what is expected for well-defined, homogenous structured states. However, the diluted-FRET approach is not sensitive to discrete, small *N,* structures. For example, consider an

extreme in which all IAPP inside the presented cell-based experiments formed dimers. The fraction of oligomers capable of contributing to events with $FRET_{eff} > 0$ would be < 0.1%. Instead, FRET is abundant in our images, with at least 70% of acceptors contributing to observation. Dilutions in this work were found empirically. For the most informative dilution in cell-based experiments, 1:1:100 (donor:acceptor:unlabeled protein), binomial statistics suggest oligomers with $N > 30$ are required for the extent of FRET observed. For the dilutions found most informative for GPMV-based experiments, 1:1:500, the estimate is $N > 150$. In order to reconcile the ease of detecting species contributing to FRET and the narrowness of the resultant $FRET_{eff}$ distributions, signal averaging must be taking place within the confocal volume.

Membrane associated IAPP oligomers are dynamic. The signal averaging required for narrow $FRET_{eff}$ distributions can result from averaging over many oligomers, or a small number of oligomers capable of rapid rearrangement. $FRET_{eff}$ observed for IAPP amyloid fibers provides a useful standard (Figure 6A) as it represents the highest possible density of IAPP oligomer within a confocal volume. A roughly Poisson distribution of $FRET_{eff}$ is measured, i.e. the confocal volume measures significant contributions to FRET throughout the range of $FRET_{eff}$ from zero to one. The signal averaging observed for membrane associated IAPP is therefore time-based rather than a large number of alternative IAPP oligomers simultaneously occupying the confocal volume. The most physically plausible origin of time-based averaging would be dynamics within the oligomers (Figure 7A).

Membrane bound oligomers of IAPP grow in size as a result of stepwise merging of smaller oligomers. Although multiple peaks can be observed on GPMVs (Figure 5), the time evolution observed suggests each peak to be a unique species. As single peaks diminish in area, others rise and no two peaks behave as a unit (Figure 4). Moreover, confocal volumes seldom contain more than one kind of oligomer simultaneously as this would result in lateral shifts in $FRET_{eff}$. It is tempting to reconcile stepped increases in $FRET_{eff}$ as resulting from transitions in the shape of oligomers and/or the density of the IAPP within them. Two features of the $FRET_{eff}$ distributions suggest this is not the case. First, a rise in $FRET_{eff}$ is accompanied by a rise in counts (Figure 5). This is neither consistent with a change in shape nor density which would simply move the $FRET_{eff}$. Second, all transitions between peaks are on somewhat similar (minutes) time-scales (Figure 4). It is highly unlikely that several unrelated kinetic

transitions should fortuitously have similar timescales. Imagine instead that initial oligomer size is on the same order as the doping ratio of labeled to unlabeled IAPP (Figure 7A). Only 3% of 100-mer oligomers would have at least one donor and one acceptor at the two dilutions used in this work (Figure 7A). Oligomers containing donor-only labeled IAPP contribute FRET=0 to the ensemble average, reducing the overall apparent $FRET_{eff}$. By size N=400, 30% of oligomers have at least one donor/acceptor pair. I.e. there is more participation of fluorophores in FRET measurements as oligomers grow which would lead to greater counts (Figure 7B and 7C). Moreover, there is an accompanying reduction in the proportion of donor-only labeled IAPP containing oligomers. This would lead to an apparently elevated FRET. Eventually, all oligomers contain donor/acceptor pairs yielding a maximum FRET (Figure 7D). Thus, fluid-like behavior of IAPP within oligomers is sufficient to account for appearance of discrete species residing on a sequential assembly pathway.

The adoption of large pore states by IAPP reflects a change in the conformation of the IAPP oligomer. If the entirety IAPP were to adopt a maximally dense, solvent excluded conformation on or off the membrane, its volume could be approximated as 4000 $Å^3$. At this density and at a donor:acceptor:unlabeled ratio of 1:1:500 (used for GPMV experiments), an isotropic distribution of IAPP within a spherical N-mer can reach a maximum simulated $FRET_{eff}$ of 0.27 (Figure 7D). The fourth and last of the small pore associated peaks measures $FRET_{eff}$ = 0.58 (Figure 5A). Even at the doping ratio of 1:1:100 (used in cellular experiments), the maximum simulated $FRET_{eff}$ is 0.69 (Figure 7D). This sensitivity to doping ratio is also evident in real world experiments (Figure S5). Increasing protein density would allow simulations to yield higher $FRET_{eff}$, but this would not be physical. Instead, we suggest that the $FRET_{eff}$ peaks evident at values elevated above these limiting values necessitate deviation of the IAPP distribution from an isotropic sphere.

The evolution of the amyloid-hypothesis into the oligomer-hypothesis for IAPP toxicity was pioneered, in part, by the immunostained light-microscopy observation of membrane associated puncta (Gurlo et al., 2010). In contrast to efforts with Aβ peptide from Alzheimer's disease (Pham et al., 2013; Yu et al., 2009), reconstitution of IAPP oligomers in membrane-free solution has only met with relatively limited success. Recent direct evidence includes the use of electrospray ionization mass spectrometry (Young et al., 2014) and photo-induced cross-linking (Abedini et al., 2016). In both cases,

observations of oligomers up to hexamers are reported. Importantly, sequence variants that do not readily form oligomers do not readily induce cytotoxicity. The latter work goes further to characterize the secondary structure of the oligomers as not-amyloid, but does not characterize the localization of toxicity to membranes either inside or outside the cell. As membrane association of much larger assemblies appears central to the development of toxicity (Janson et al., 1999), the effort with most bearing on our work here is a reconstitution study in which SDS was used as a membrane model (Bram et al., 2014). The resultant oligomer was toxic, chromatographically stable, discrete in size (~90kDa), rich in α-helical secondary structure, shown to enter cells and localize to mitochondria. Remarkably, anti-sera from diabetic patients but not controls were cross reactive with this oligomer, but not monomer and not fibers. The 90kDa size and subcellular localization observed in that work is consistent with the observations reported here. Moreover, ADM-116 specifically binds and stabilizes the α-helical membrane binding sub-domain of IAPP(Kumar et al., 2016b). We do not exclude the possibility that the large species observed on membranes requires early steps of dimer through hexamer formation. Rather, we assert that there exist multiple, well-defined forms of these much larger oligomers, associated with sub-cellular membranes, that are responsible for gains-in-toxic function.

Second phase and not first phase poration by IAPP is associated with toxicity. Oligomers of IAPP have been implicated in toxic mechanisms that include membrane poration, ER stress, and failures of any of several degradative proteostatic systems (Mukherjee A, 2015). Our approach here leverages IAPP's cell penetrating qualities to focus on intracellular poration (Kumar et al., 2016b). An alternative approach is transgenic overexpression of IAPP (Matveyenko and Butler, 2006). The two approaches differ with respect to observations at the ER, but both show correlation of mitochondrial localization with cell death. Importantly, mitochondrial poration need not be toxic. Indeed, recent work with the mitochondrial protonophore, DNP, shows that poration of the mitochondria can be protective (Perry et al., 2015). Here, DNP mediated poration could be observed when applied to lumen labeled GPMVs (Figure 1D). The observation of a single kinetic phase that does not go to baseline is consistent with small hole poration observed using IAPP (Figure 1E, 1H and S2). The non-amyloidogenic sequence variant of IAPP from rats is only weakly toxic requiring ~100 fold greater concentrations to affect INS-1 cells (Magzoub and Miranker, 2012). On GPMVs, rIAPP, even at 40:1 protein to lipid ratio, shows

predominantly only first phase, small hole leakage (Figure 1G). Thus, under three distinct non-toxic conditions, DNP, rIAPP and rescue from hIAPP toxicity using ADM-116, only first-phase, small hole permeation is present. One way to explain small hole formation by IAPP oligomers is to imagine it forms a selective mesh. This would be akin to functional biological systems including, for example, the FG domains present within the nuclear pore complex (Hulsmann et al., 2012).

Our work here has shown not only the existence of multiple oligomeric states, but that these states are sufficiently well-defined as to be distinguishable by structure-specific small-molecule binding. While we have not shown phase transitions or boundaries, the dynamic nature measured here for IAPP oligomers places them in the same discourse as protein liquid droplet formation. Such behavior for proteins associated with membranes has been noted before. For example, Nephrin (Banjade and Rosen, 2014) and more recently LAT (Su et al., 2016) which forms micron sized clusters during T-cell activation. Indeed, fluid-phase separation was already a property established by us for IAPP in solution (Padrick and Miranker, 2002); (Rhoades and Gafni, 2003). We are only now coming to appreciate that this property may be meaningful in a cellular membrane context. A phase separation framework allows a rethinking of the nature of small molecule interactions with such systems. It can account, for example, for the fact that ADM-116 is a structure specific binder and yet can function at substoichiometic ratios (Kumar et al., 2016b). ADM-116 is therefore a proof-of-concept to the idea that changes to protein liquid droplet formation are addressable by small molecule development for basic and translational research.

Author contributions

M.B., E.R, and A.D.M. designed the project and experiments. M.B. performed the experiments. M.B., E.R., and A.D.M, analyzed the data and wrote the manuscript. S.K. synthesized the oligoquinoline amides.

Acknowledgements

This research was supported by NIH GM094693 (to A.D.M.), GM102815 (to A.D.M. and E.R.) and an American Diabetes Association mentor-based postdoctoral fellowship to M.B. We thank Alex Miranker for assistance with programming diluted-FRET simulations and Dr J. Wolenski for technical assistance with microscopy.

Additional information

Competing financial interests: The authors declare no competing financial interests.

References

Abedini, A., Plesner, A., Cao, P., Ridgway, Z., Zhang, J., Tu, L.H., Middleton, C.T., Chao, B., Sartori, D.J., Meng, F., *et al.* (2016). Time-resolved studies define the nature of toxic IAPP intermediates, providing insight for anti-amyloidosis therapeutics. eLife *5*.

Aguzzi, A., and Altmeyer, M. (2016). Phase Separation: Linking Cellular Compartmentalization to Disease. Trends in cell biology *26*, 547-558.

Antonenko, Y.N., Khailova, L.S., Knorre, D.A., Markova, O.V., Rokitskaya, T.I., Ilyasova, T.M., Severina, II, Kotova, E.A., Karavaeva, Y.E., Prikhodko, A.S., *et al.* (2013). Penetrating cations enhance uncoupling activity of anionic protonophores in mitochondria. PloS one *8*, e61902.

Banjade, S., and Rosen, M.K. (2014). Phase Transitions of Multivalent Proteins Can Promote Clustering of Membrane Receptors. eLife *3*.

Bram, Y., Frydman-Marom, A., Yanai, I., Gilead, S., Shaltiel-Karyo, R., Amdursky, N., and Gazit, E. (2014). Apoptosis induced by islet amyloid polypeptide soluble oligomers is neutralized by diabetes-associated specific antibodies. Sci Rep-Uk *4*.

Brangwynne, C.P., Mitchison, T.J., and Hyman, A.A. (2011). Active liquid-like behavior of nucleoli determines their size and shape in Xenopus laevis oocytes. Proceedings of the National Academy of Sciences of the United States of America *108*, 4334-4339.

Brender, J.R., Lee, E.L., Cavitt, M.A., Gafni, A., Steel, D.G., and Ramamoorthy, A. (2008). Amyloid fiber formation and membrane disruption are separate processes localized in two distinct regions of IAPP, the type-2-diabetes-related peptide. Journal of the American Chemical Society *130*, 6424-6429.

Costes, S., Langen, R., Gurlo, T., Matveyenko, A.V., and Butler, P.C. (2013a). beta-Cell Failure in Type 2 Diabetes: A Case of Asking Too Much of Too Few? Diabetes *62*, 327-335.

Costes, S., Langen, R., Gurlo, T., Matveyenko, A.V., and Butler, P.C. (2013b). beta-Cell failure in type 2 diabetes: a case of asking too much of too few? Diabetes *62*, 327-335.

Courchaine, E.M., Lu, A., and Neugebauer, K.M. (2016). Droplet organelles? The EMBO journal *35*, 1603-1612.

Cremers, C.M., Knoefler, D., Gates, S., Martin, N., Dahl, J.U., Lempart, J., Xie, L., Chapman, M.R., Galvan, V., Southworth, D.R., *et al.* (2016). Polyphosphate: A Conserved Modifier of Amyloidogenic Processes. Molecular cell *63*, 768-780.

Elbaum-Garfinkle, S., Ramlall, T., and Rhoades, E. (2010). The role of the lipid bilayer in tau aggregation. Biophys J *98*, 2722-2730.

Gao, M., and Winter, R. (2015). The Effects of Lipid Membranes, Crowding and Osmolytes on the Aggregation, and Fibrillation Propensity of Human IAPP. Journal of diabetes research *2015*, 849017.

Gurlo, T., Ryazantsev, S., Huang, C.J., Yeh, M.W., Reber, H.A., Hines, O.J., O'Brien, T.D., Glabe, C.G., and Butler, P.C. (2010). Evidence for proteotoxicity in beta cells in type 2 diabetes: toxic islet amyloid polypeptide oligomers form intracellularly in the secretory pathway. The American journal of pathology *176*, 861-869.

Hulsmann, B.B., Labokha, A.A., and Gorlich, D. (2012). The Permeability of Reconstituted Nuclear Pores Provides Direct Evidence for the Selective Phase Model. Cell *150*, 738-751.

Janson, J., Ashley, R.H., Harrison, D., McIntyre, S., and Butler, P.C. (1999). The mechanism of islet amyloid polypeptide toxicity is membrane disruption by intermediate-sized toxic amyloid particles. Diabetes *48*, 491-498.

JW. Krieger, J.L. (2015). QuickFit 3.0: A data evaluation application for biophysics. In http://wwwdkfzde/Macromol/quickfit/.

Kegulian, N.C., Sankhagowit, S., Apostolidou, M., Jayasinghe, S.A., Malmstadt, N., Butler, P.C., and Langen, R. (2015). Membrane Curvature-sensing and Curvature-inducing Activity of Islet Amyloid Polypeptide and Its Implications for Membrane Disruption. The Journal of biological chemistry *290*, 25782-25793.

King, E.J. (1932). The colorimetric determination of phosphorus. The Biochemical journal *26*, 292-297.

Knight, J.D., Hebda, J.A., and Miranker, A.D. (2006). Conserved and cooperative assembly of membrane-bound alpha-helical states of islet amyloid polypeptide. Biochemistry *45*, 9496-9508.

Knowles, T.P., Vendruscolo, M., and Dobson, C.M. (2014). The amyloid state and its association with protein misfolding diseases. Nature reviews Molecular cell biology *15*, 384-396.

Kumar, S., Birol, M., and Miranker, A.D. (2016a). Foldamer scaffolds suggest distinct structures are associated with alternative gains-of-function in a preamyloid toxin. Chemical communications *52*, 6391-6394.

Kumar, S., Birol, M., Schlamadinger, D.E., Wojcik, S.P., Rhoades, E., and Miranker, A.D. (2016b). Foldamer-mediated manipulation of a pre-amyloid toxin. Nature communications *7*, 11412.

LeVine, H., 3rd (1993). Thioflavine T interaction with synthetic Alzheimer's disease beta-amyloid peptides: detection of amyloid aggregation in solution. Protein science : a publication of the Protein Society *2*, 404-410.

Magzoub, M., and Miranker, A.D. (2012). Concentration-dependent transitions govern the subcellular localization of islet amyloid polypeptide. FASEB journal : official publication of the Federation of American Societies for Experimental Biology *26*, 1228-1238.

Matveyenko, A.V., and Butler, P.C. (2006). Islet amyloid polypeptide (IAPP) transgenic rodents as models for type 2 diabetes. Ilar J *47*, 225-233.

Mukherjee A, M.-S.D., Butler PC, Soto C. (2015). Type 2 Diabetes as a Protein Misfolding Disease. . Trends in molecular medicine *21*, 439-449.

Mukherjee, A., Morales-Scheihing, D., Butler, P.C., and Soto, C. (2015). Type 2 diabetes as a protein misfolding disease. Trends Mol Med *21*, 439-449.

Nath, A., Miranker, A.D., and Rhoades, E. (2011). A membrane-bound antiparallel dimer of rat islet amyloid polypeptide. Angewandte Chemie *50*, 10859-10862.

Padrick, S.B., and Miranker, A.D. (2002). Islet amyloid: Phase partitioning and secondary nucleation are central to the mechanism of fibrillogenesis. Biochemistry *41*, 4694-4703.

Perry, R.J., Zhang, D., Zhang, X.M., Boyer, J.L., and Shulman, G.I. (2015). Controlled-release mitochondrial protonophore reverses diabetes and steatohepatitis in rats. Science *347*, 1253-1256.

Pham, J.D., Chim, N., Goulding, C.W., and Nowick, J.S. (2013). Structures of oligomers of a peptide from beta-amyloid. Journal of the American Chemical Society *135*, 12460-12467.

Podkalicka, J., Biernatowska, A., Majkowski, M., Grzybek, M., and Sikorski, A.F. (2015). MPP1 as a Factor Regulating Phase Separation in Giant Plasma Membrane-Derived Vesicles. Biophys J *108*, 2201-2211.

Rhoades, E., and Gafni, A. (2003). Micelle formation by a fragment of human islet amyloid polypeptide. Biophys J *84*, 3480-3487.

Roszik, J., Lisboa, D., Szollosi, J., and Vereb, G. (2009). Evaluation of intensity-based ratiometric FRET in image cytometry--approaches and a software solution. Cytometry Part A : the journal of the International Society for Analytical Cytology *75*, 761-767.

Schlamadinger, D.E., and Miranker, A.D. (2014). Fiber-dependent and -independent toxicity of islet amyloid polypeptide. Biophys J *107*, 2559-2566.

Schneider, C.A., Rasband, W.S., and Eliceiri, K.W. (2012). NIH Image to ImageJ: 25 years of image analysis. Nature methods *9*, 671-675.

Seeliger, J., Weise, K., Opitz, N., and Winter, R. (2012). The effect of Abeta on IAPP aggregation in the presence of an isolated beta-cell membrane. Journal of molecular biology *421*, 348-363.

Sezgin, E., Kaiser, H.J., Baumgart, T., Schwille, P., Simons, K., and Levental, I. (2012). Elucidating membrane structure and protein behavior using giant plasma membrane vesicles. Nat Protoc *7*, 1042-1051.

Soty M, V.M., Soriano S, del Carmen Carmona M, Nadal Á, Novials A. (2011). Involvement of ATP-sensitive Potassium (KATP) Channels in the Loss of Beta-cell Function Induced by Human Islet Amyloid Polypeptide. The Journal of biological chemistry *286*, 40857-40866.

Su, X., Ditlev, J.A., Hui, E., Xing, W., Banjade, S., Okrut, J., King, D.S., Taunton, J., Rosen, M.K., and Vale, R.D. (2016). Phase separation of signaling molecules promotes T cell receptor signal transduction. Science *352*, 595-599.

Wimley, W.C. (2010). Describing the mechanism of antimicrobial peptide action with the interfacial activity model. ACS chemical biology *5*, 905-917.

Young, L.M., Cao, P., Raleigh, D.P., Ashcroft, A.E., and Radford, S.E. (2014). Ion mobility spectrometry-mass spectrometry defines the oligomeric intermediates in amylin amyloid formation and the mode of action of inhibitors. Journal of the American Chemical Society *136*, 660-670.

Yu, L., Edalji, R., Harlan, J.E., Holzman, T.F., Lopez, A.P., Labkovsky, B., Hillen, H., Barghorn, S., Ebert, U., Richardson, P.L.*, et al.* (2009). Structural characterization of a soluble amyloid beta-peptide oligomer. Biochemistry *48*, 1870-1877.

METHODS

Materials. Chemicals were purchased from Sigma Aldrich (St. Louis, MO) unless otherwise specified. Thioflavin T (ThT) was purchased from Acros Organics (Fair Lawn, NJ) and islet amyloid polypeptide (IAPP) from Elim Biopharmaceuticals (Hayward, CA, USA). ADM-116 was previously prepared as described (Kumar et al., 2016a). IAPP stocks were prepared by solubilizing ~2mg protein in 7 M guanidinium hydrochloride. The solution was filtered (0.2 micron) and transferred to C-18 spin column, washed twice with water followed by a wash of 10% acetonitrile, 0.1% formic acid (v/v) and then eluted into 200 µL of 50% acetonitrile, 0.1% formic acid (v/v). The concentration of IAPP was determined by OK at 280 nm (ε = 1400 $M^{-1}cm^{-1}$). The solution was then divided into single use aliquots (20-50 µL), lyophilised, and stored at -80 ºC. Stock solutions of IAPP were prepared with water from these aliquots. Alexa 488 carboxylic acid succinimidyl ester (A488), Atto 647N succinimidyl ester (A647) and Alexa 594 succinimidyl ester (A594) dyes were purchased from Life Technologies (Carlsbad, CA). IAPP labelling was prepared as described previously (Magzoub and Miranker, 2012). Briefly, IAPP was incubated with dye, succinimidyl ester on a MacroSpin column for 4 h. Labelled IAPP was eluted from the MacroSpin column with 50% acetonitrile/0.2% formic acid solution. This was then diluted with 7 M guanidinium hydrochloride solution to a total organic content of <5%. Labelled protein was then purified by reverse-phase high-performance liquid chromatography, and identity was confirmed by mass spectrometry. Aliquots were lyophilized and stored at −80°C. Stocks at 100 μM in water were prepared and immediately before use. IAPP control fibers were prepared by incubating 50 μM hIAPP and 100 nM $IAPP_{A647}$ in 50 mM sodium phosphate buffer, 100 mM KCl, pH 7.4, for ∼24 h. Fibers were pelleted at 21,000 *g* for 30 min and resuspended three times using water..

Giant Plasma Membrane Vesicles. GPMVs were isolated from INS-1 cells as previously described (Schlamadinger and Miranker, 2014). Briefly, cells were plated in 35 mm dishes and cultured for 48 h, washed with a 10 mM HEPES, 150 mM NaCl, 2 mM $CaCl_2$ (pH = 7.4) twice and then exposed to 10 mM N-ethyl maleimide (NEM, Sigma Aldrich, St. Louis, MI, USA) for 2 h. Collected samples were then passed over a gravity-flow column (Bio-Rad) containing size exclusion Sephacryl of pore size 400-HR (Sigma Aldrich, St. Louis, MI, USA) to separate GPMVs from residual cell debris. For leakage assays, the thiol-reactive fluorescent probe, CellTracker Orange (Thermo Scientific, Rochester, NY,

USA) was first applied to cells at 1:1000 dilution and incubated for 1 h at 37 ^{o}C. The phospholipid content of unlabeled and labeled final material was measured by total phosphate assay.

GPMV Imaging. Images were obtained in 8-well NUNC chambers (Thermo Scientific, Rochester, NY, USA) containing 250 µl of GMPV at 5 µM phospholipid lipid concentration. Imaging was carried out at the Yale Department of Molecular, Cellular, and Developmental Biology imaging facility, on a Zeiss LSM 510 confocal microscope, using a 63x Plan-Apo/1.4-NA oil-immersion objective with DIC capability (Carl Zeiss, Oberkochen, Germany). Image acquisition and processing were achieved using Zeiss Efficient Navigation (ZEN) and Image J software (Schneider et al., 2012).

Fluorescence correlation spectroscopy (FCS). FCS measurements were made on an LSM 880 Airyscan system NLO/FCS Confocal microscope (Carl Zeiss, Oberkochen, Germany) with a C-Apochromat 40×/1.2 NA UV-VIS-IR Korr. water immersion objective (Carl Zeiss, Oberkochen, Germany). Thiol-conjugated molecules were excited at 594 nm. Confocal pinhole diameter was adjusted to 70 µm. Emission signals were detected through a 607-nm long-pass filter. Measurements were made in 8-well chambered coverglasses (Nunc, Rochester, NY, USA). All samples were incubated in GPMV buffer (10 mM HEPES, 150 mM NaCl, 2 mM $CaCl_2$ (pH = 7.4)) for 1 h prior to taking measurements. Autocorrelation data were collected at regular intervals (5 min) with each autocorrelation curve collected over 10 s with 30 repeats.

Autocorrelations were fit using the software QuickFit3.0 (JW. Krieger, 2015). For thiol-conjugates, a model for a single diffusing species undergoing 3D Brownian diffusion was used.

$$G(\tau) = \frac{1}{\mathrm{N}} \times \left[1 + \frac{\tau}{\tau_{d,1}}\right]^{-1} \times \left[1 + \frac{\tau}{s^2\tau_{d,1}}\right]^{-\frac{1}{2}} \quad (1)$$

Here, N is the total thiol-conjugated molecules in the detection volume. The characteristic translational diffusion time of a diffusing particle is given by $\tau_{d,1}$. The structure factor, s, was determined as a free parameter for solutions of free Alexa 594 hydrazide dye and then fixed to the experimentally determined value of 0.1 for all subsequent fittings. For experiments of conjugates eluting during the second decay phase of leakage diffusion was assessed by burst counts within the time frame analysed.

Confocal microscopy, cell imaging. Images were obtained in 8-well NUNC chambers (Thermo Scientific, Rochester, NY, USA) seeded with 20000 - 25000 cells/well. Cells were cultured for 48 h after passage before beginning experiments. For time dependent colocalization experiments of IAPP with JC-1 mitochondrial staining, the medium contained 200 nM $IAPP_{A647}$, 13 μM unlabelled peptide. For experiments in the presence of ADM-116, 13 μM of molecule was introduced in the medium following a 3 h incubation of cells with IAPP. For experiments monitoring mitochondria, JC-1 was incubated with cells at 1:5000, at 37 ^{o}C for 45 minutes prior to addition of protein. Images were acquired after 48 h total incubation time. Imaging was carried out using a x100 Plan-Apo/1.4-NA oil-immersion objective with DIC capability (Carl Zeiss, Oberkochen, Germany). For all experiments reporting on the colocalization of labelled IAPP, the gain setting for the blue channel was kept constant from sample to sample. Mitochondria containing JC-1 aggregates were detected in red (excitation 540 nm, emission 570 nm), and monomers in the green channel (excitation 490 nm, emission 520 nm). Image acquisition and processing were achieved using Zeiss Efficient Navigation (ZEN) and Image J software (Schneider et al., 2012).

Intracellular imaging Förster resonance energy transfer (FRET). The INS-1 growth media was replaced with media containing 100 nM $IAPP_{A488}$ and 100 nM $IAPP_{A647}$ (or 100 nM $IAPP_{A594}$) and unlabelled IAPP and incubated for the time scales indicated in the text. Media was replaced with fresh prior to imaging. In experiments where ADM-116 was used, small molecule was added 3 h after incubation with protein. Images were acquired using a 100x Plan-Apo/1.4-NA oil-immersion objective with DIC capability (Carl Zeiss, Oberkochen, Germany). For the donor channel, $IAPP_{A488}$ was excited with a 488 nm Argon2 laser and detected through a 505/550 nm emission filter. For the acceptor channel, $IAPP_{A647}$ was excited with a 633 Argon2 laser and detected through a 730/750-nm emission filter. For all experiments the pinhole was kept constant to the Z-slice thickness of each filter channel. Single cell images were obtain for donor alone, acceptor alone and donor-acceptor fusion channels. Image acquisition and processing were achieved using Zeiss Efficient Navigation (ZEN) and Image J software (Soty M, 2011). The Image J plugin, RiFRET (Roszik et al., 2009), was used to calculate and remove the bleed through for each channel and to calculate a pixel-based FRET efficiency. The FRET distance was then calculated using:

$$E = \frac{R_0^6}{R_0^6 + r^6} \quad (4)$$

Where E is the calculated efficiency of FRET energy transfer, R_0 is the Förster distance and r is the distance between the donor and the acceptor.

Imaging FRET. GPMV experiments were conducted in 8-well NUNC chambers (Thermo Scientific, Rochester, NY, USA) including 250 µl of GMPV stock solution at 5 µM apparent phospholipid (in monomer units). Wells containing GPMVs were mixed with 100 nM $IAPP_{A488}$ and 100 nM $IAPP_{A647}$ (or 100 nM $IAPP_{A594}$) and unlabelled IAPP. In experiments where ADM-116 was used, small molecule was added at the same time as protein. The same microscope setup and analysis procedure was used to image FRET in GPMVs and cells.

Cell culture. Rat insulinoma INS-1 cells (832/13, Dr. Gary W. Cline, Department of Internal Medicine, Yale University) were cultured at 37ºC and 5% CO_2 in phenol red free RPMI 1640 media supplemented with 10% fetal bovine serum, 1% penicillin/streptomycin (Life Technologies, Carlsbad, CA, USA), and 2% INS-1 stock solution (500 mM HEPES, 100 mM L-glutamine, 100 mM sodium pyruvate, and 2.5 mM β-mercaptoethanol). Cells were passaged upon reaching ~95% confluence (0.25% Trypsin-EDTA, Life Technologies), propagated, and/or used in experiments. Cells used in experiments were pelleted and resuspended in fresh media with no Trypsin-EDTA.

Cell Viability. Cell viability was measured colorimetrically using the Cell-Titer Blue (CTB, Promega, Madison, WI, USA) fluorescence-based assay. Cells were plated at a density 5000 cells/well in 96-well plates (BD Biosciences, San Diego, CA). Peptide was directly introduced to each well after 48 h of culture and then incubated for an additional 48 h. For time dependent experiments, cells were incubated with peptide for the specified time points. After the incubation period, 20 µL CTB reagent was added to each well and incubated at 37°C and 5% CO_2 for 2.5 – 3.5 h. Fluorescence of the resorufin product was measured on a FluoDia T70 fluorescence plate reader (Photon Technology International, Birmingham, NJ, USA). All wells included the same amount of water to account for different concentrations of peptide added to sample wells. Wells that included water vehicle but not peptide served as the negative control (0% toxic), and wells containing 10% DMSO were the positive control (100% toxic). Percent toxicity was calculated using the following equation:

$$\%Toxicity = 100 - [100 \cdot \left(\frac{<S>-<P>}{<N>-<P>}\right)] \quad (5)$$

Each independent variable is the average of eight plate replicates from the negative control (<*N*>), positive control (<*P*>), and samples (<*S*>). Results presented for viability experiments are an average of three such experiments conducted independently on different days. Error bars represent the standard error of the mean.

Phosphate assay. Lipid concentrations for GPMV preparations were determined by measuring total phosphate (King, 1932), assuming that all measured phosphate is from phospholipids, and that all lipids are phospholipids. This is a practical assumption designed to ensure reproducibility.

Simulation of diluted-FRET. Expected values of $FRET_{eff}$ for dynamic, isotropic distributions of spherically distributed IAPP were computed by numerical integration coded in-house using Mathematica (Wolfram Research, Champaign, IL). Briefly, the experimental ratio of labeled to unlabeled protein defines a binomial probability for the number of fluorophores distributed within trial spheres. The size of the spheres was dictated by constants (stated in the main text) for protein density and the total number of placed protein molecules. Spherical oligomers were generated randomly until the cumulative $FRET_{eff}$ converged to a single value. Occurrences of multiple acceptors and donors within a single oligomer were accommodated by treating each potential dye pair, *ij*, as having an independent probability of resonance transfer, p_{ij}. For example, a trial oligomer containing a single donor and three acceptors located a distance of R_o away gives a $FRET_{eff}$ =0.875. Effects of donor-donor and acceptor-acceptor interactions were not considered. In general, multi-fluorophore corrections contribute negligibly to computations performed at the experimental ratios used in this work (Figure 7D).

Figures

Figure 1

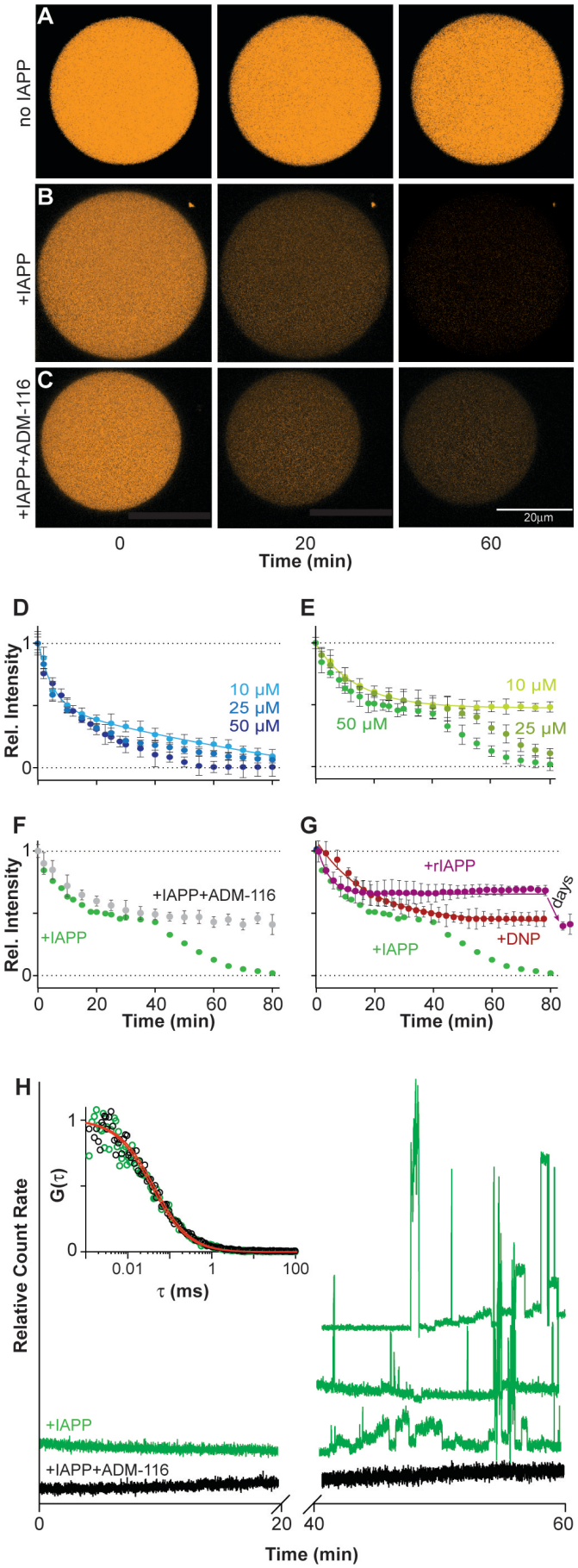

Figure 1: IAPP induces poration of a cell derived membrane

(A-C) Representative confocal imaging of CellTracker Orange labeled GPMVs at the indicated time-points. Shown are single GPMVs observed without added IAPP (A), IAPP added to a ratio of 10:1, IAPP:lipid (B), or IAPP and ADM-116 added at a ratio of 10:1:10 (IAPP:lipid:ligand) (C).

(D-G) Integration of intensities across repeats of data as in (A-C) used to compute kinetic profiles of leakage from 5 μM (phospholipid monomer units) GPMVs. Error bars are standard deviations from three sets of experiments conducted on separate occasions.

(D, E) Leakage profiles after addition of the indicated concentrations of IAPP in the presence and absence of 1 mM AB9 respectively.

(F) Leakage profile at 50 μM IAPP in the presence of equimolar ADM-116. Corresponding data in the absence of ADM-116, (E), is shown as overlay.

(G) Leakage profiles upon addition of 10 μM DNP or 200 μM of the sequence variant of IAPP from rats, rIAPP. Corresponding data for 50 μM human IAPP, (E), is shown as overlay.

(H) Monitoring the diffusion of fluorescent material escaping the GPMV lumen by FCS. Representative traces of photon bursts are measured monitored over time in the absence (green) and presence of ADM-116 (black) under conditions matched to (F). Inset: autocorrelation overlayed with fits for data from the first 20 minutes. Right: Three repeats of bursts recorded at time 40 to 60 mins for protein in the absence of ADM-116 are shown.

See also Figure S1.

Figure 2

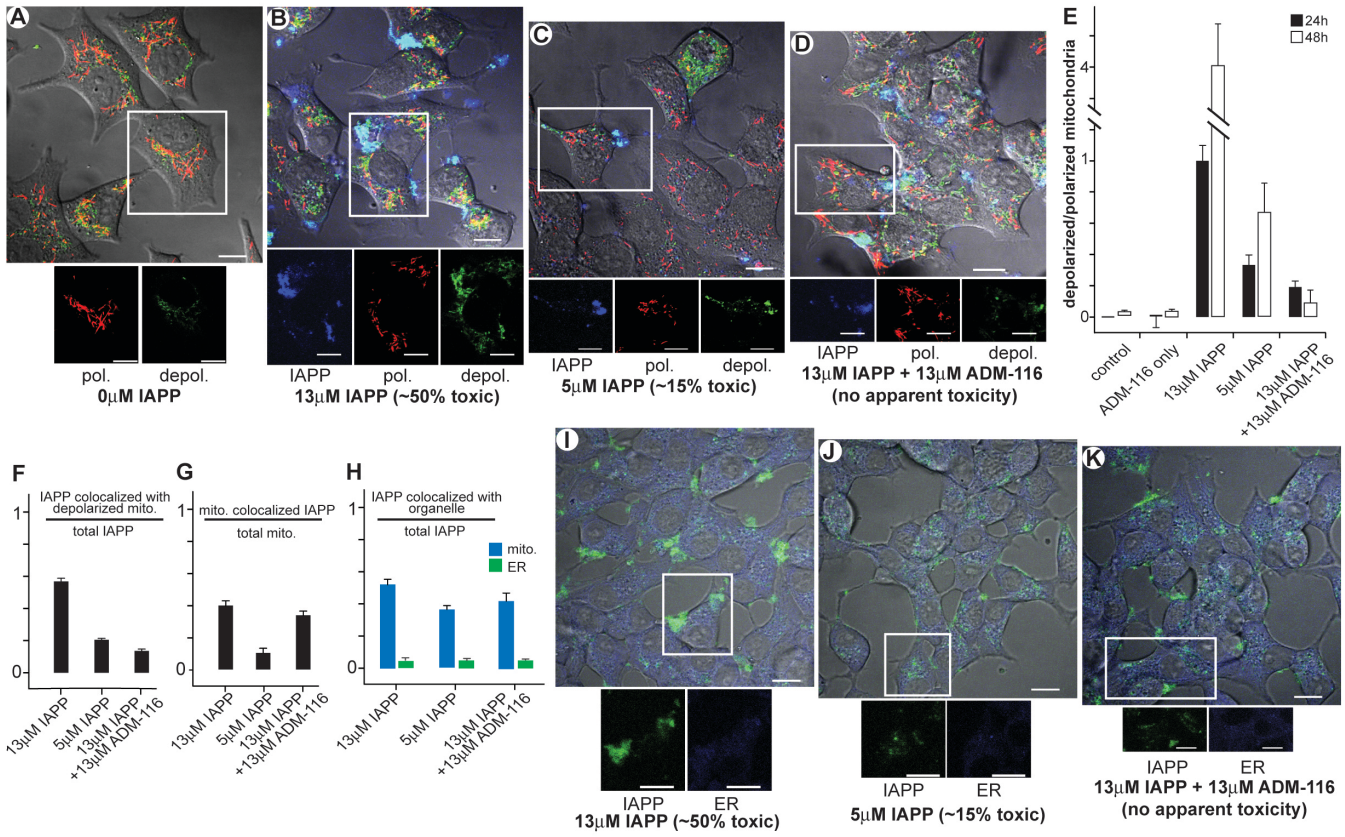
A
pol.
depol.
0μM IAPP
B
IAPP
pol.
depol.
13μM IAPP (~50% toxic)
C
IAPP
pol.
depol.
5μM IAPP (~15% toxic)
D
IAPP
pol.
depol.
13μM IAPP + 13μM ADM-116
(no apparent toxicity)
E
24h
48h
depolarized/polarized mitochondria
control
ADM-116 only
13μM IAPP
5μM IAPP
13μM IAPP +13μM ADM-116
F
IAPP colocalized with depolarized mito.
total IAPP
G
mito. colocalized IAPP
total mito.
H
IAPP colocalized with organelle
total IAPP
mito.
ER
13μM IAPP
5μM IAPP
13μM IAPP +13μM ADM-116
I
IAPP
ER
13μM IAPP (~50% toxic)
J
IAPP
ER
5μM IAPP (~15% toxic)
K
IAPP
ER
13μM IAPP + 13μM ADM-116
(no apparent toxicity)

Figure 2: Mitochondria colocalized IAPP is associated with depolarization

(A) Representative INS-1 cells stained with JC-1 marker. Two fluorescence channels in red and green correspond to polarized and depolarized mitochondria respectively. These are shown merged with the differential interference contrast (DIC) image. A region of interest (ROI) is chosen to show channels individually.

(B) Representative cells exposed to toxic (13 μM) concentrations of IAPP doped with 200 nM $IAPP_{A647}$ for imaging. Cells were stained with JC-1 marker 24 h after IAPP. The three channels, $IAPP_{A647}$ (blue), polarized (red) and depolarized (green) mitochrondria are shown merged with the DIC image. A region of interest (ROI) is chosen to show channels individually.

(C) As in Figure 2B but at 5 μM IAPP.

(D) As in Figure 2B, but with the addition of 13 μM ADM-116 three hours after IAPP.

(E) Image overlap statistics for Figure 2A-D showing ratio of depolarized/polarized mitochondria under the indicated conditions and incubation time.

(F) Image overlap statistics for Figure 2B-D showing fraction of total IAPP overlapping depolarized mitochondria.

(G) Image overlap statistics for Figure 2B-D showing fraction of total mitochondria colocalized with IAPP.

(H) Image overlap statistics for Figure 2B-D and Figure 2I-K, showing fraction of total IAPP overlapping with mitochondria and ER respectively.

(E-H) For each measurement a total of 50 cells were selected for analysis from 3 biological replicates. Error bars are standard deviations from each conditions set of cells.

(I-K) As in Figure 2B-D, but monitoring using ER-Tracker instead of mitochondrial polarization and doping IAPP with 200 nM $IAPP_{A488}$.

Scale bar for all images is 20 μm.

See also Figures S2 and S3.

Figure 3

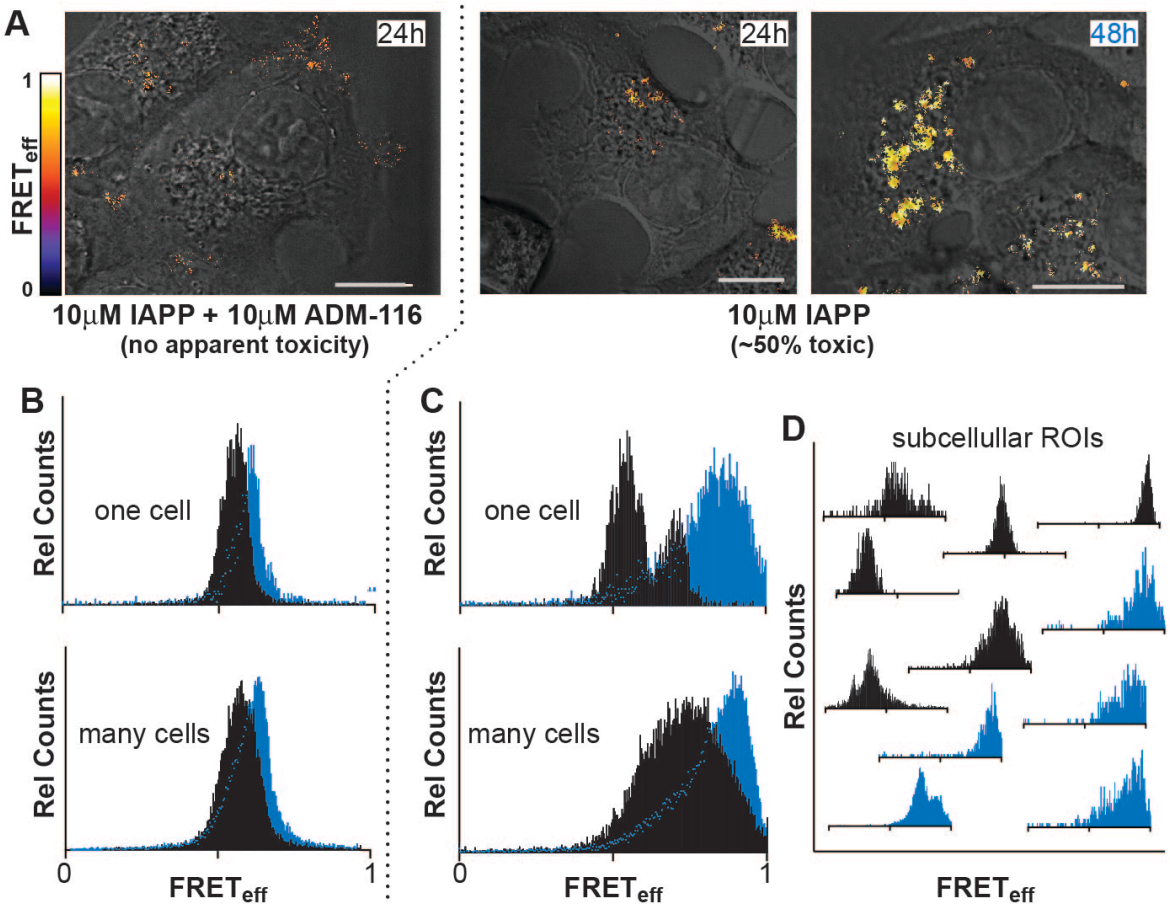

Figure 3: IAPP adopts a specific conformation in cells upon rescue

(A) Intermolecular FRET between $IAPP_{A488}$ and $IAPP_{A647}$ (in the presence of unlabeled IAPP, 1:1:100) imaged in live INS-1 cells under the conditions indicated. For left image, note that ADM-116 is added 3 h after IAPP (see main text). Pixel-based FRET analysis of representative ROIs are shown as a heat map merged with corresponding DIC images. Scale bar, 10 μm.

(B-D) Histograms of pixel counts for $FRET_{eff}$ images as in (A).

(B) $FRET_{eff}$ histograms for cells at 24 h (black) and 48 h (cyan) for the rescued condition (A). Analysis for a representative single cell is shown above the sum of data collected from 50 cells from 3 independently conducted experiments on each of 3 different days.

(C) Analysis as in (B), under conditions (10 μM IAPP) in which ~50% toxicity is measured colorimetrically (Figure S2).

(D) Analysis as in (C), but for representative ROIs within and far smaller than single cells.

See also Figures S2 and S4.

Figure 4

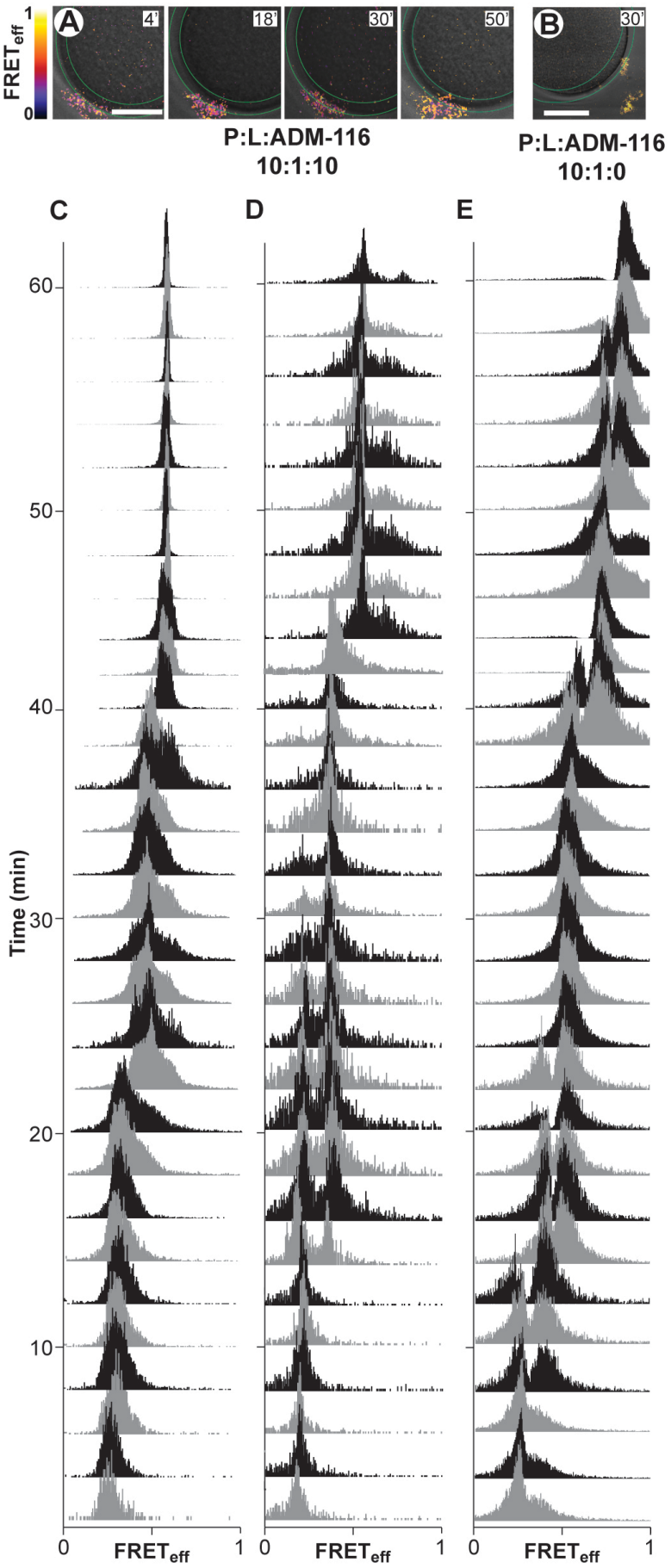
FRET$_{eff}$
1
0
A
4'
18'
30'
50'
B
30'
P:L:ADM-116
10:1:10
P:L:ADM-116
10:1:0
C
D
E
Time (min)
60
50
40
30
20
10
0
FRET$_{eff}$
1

Figure 4: Time resolved conformational changes of IAPP on GPMVs match leakage profiles

Time dependent changes to intermolecular FRET between $IAPP_{A488}$ and $IAPP_{A647}$ (in the presence of unlabeled IAPP, 1:1:500) imaged on GPMVs and shown as a heat map merged with corresponding DIC images. Below these, image statistics are shown as histograms of pixel counts.

(A, B) Representative time points of a single ring shaped ROI (green) that predominantly includes the membrane. GPMVs at 5 μM (phospholipid monomer units) incubated with IAPP, lipid and ADM-116 at the indicated ratios. Scale bar, 10 μm.

(C-E) $FRET_{eff}$ histograms from single optical sections of a single GMPV monitored over time after exposure to IAPP and ADM-116 at ratios of 10:1:10 (C), 5:1:0 (D) and 10:1:0 (E). Images were recorded every 2' using ring-shaped ROIs that encompass the membrane.

See also Figure S4.

Figure 5

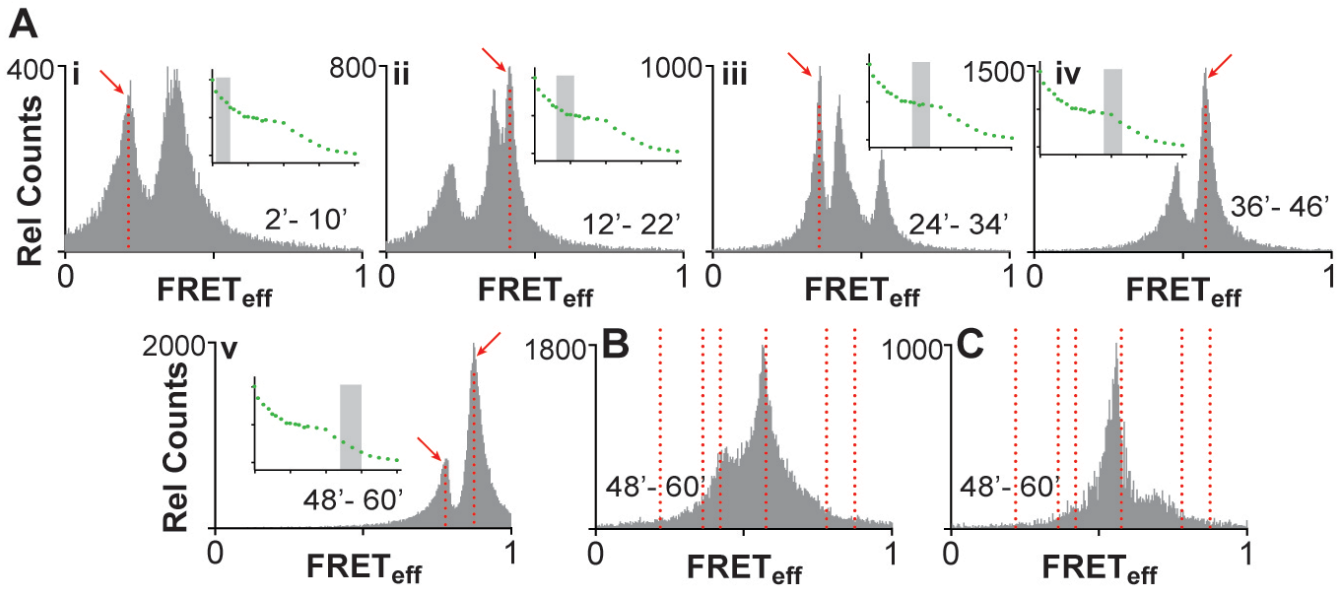

Figure 5: Global changes to IAPP oligomers on GPMVs

Intermolecular FRET histograms from analyses conducted as in Figure 4, but integrated over 5 optical sections for each GPMV, a minimum of 3 GPMVs and the indicated spans of time.

Time dependent changes to intermolecular FRET between $IAPP_{A488}$ and $IAPP_{A647}$ (in the presence of unlabeled IAPP, 1:1:500)

(A) Under conditions matched to Figure 4E, histograms are shown (*i*-*v*) corresponding to summation across the indicated time period. Red arrows indicate peaks that define $FRET_{eff}$ values for species referred to in the main text and the locations of dotted red lines in (B, C) and Figure 6A. Inset: Schematic of leakage profile collected under matched conditions (Figure 1F) except for omission of fluorophore labeled IAPP. Grey rectangles corresponds to the integrated time period relevant to the associated $FRET_{eff}$ histogram.

(B, C) As in (A), but corresponding to IAPP, lipid and ADM-116 at ratios of 10:1:10 (B) and 5:1:0 (C). These correspond to conditions in Figure 4C and 4D respectively.

Figure 6

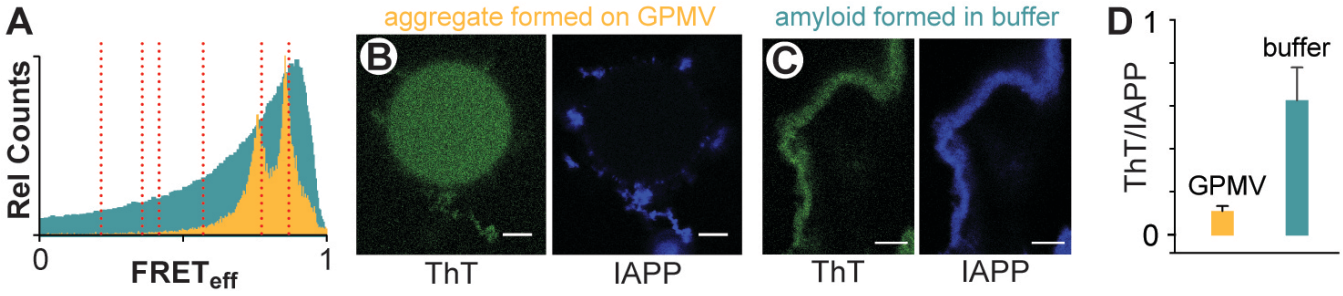

Figure 6: IAPP oligomers on GPMVs do not have a canonical amyloid fiber structure

(A) Intermolecular $FRET_{eff}$ statistics from 50 ROIs of aggregates prepared using $IAPP_{A488}$, $IAPP_{A647}$ and unlabeled IAPP (1:1:500). GPMV associated aggregates (orange) were prepared under conditions matched to Figure 5A with ROIs taken at 60' timepoints and at locations distal from the GPMV surface. Amyloid fibers prepared as control in aqueous buffer are shown in cyan.

(B, C) Confocal imaging of IAPP aggregates prepared from IAPP doped with $IAPP_{A647}$ (500:1) and further stained with the amyloid indicator dye, ThT. Two channel image pairs are shown for ThT (green) and $IAPP_{A647}$ (blue) respectively. Aggregates were prepared either in the presence of GPMVs (B) or in aqueous buffer (C).

(D) Imaging statistics for data as in (B, C). Presented as the ratio of ThT intensities divided by $IAPP_{A647}$ intensities using ROIs away from the GPMV surface. Error bars are standard deviations from three sets of experiments conducted on independent occasions.

Figure 7

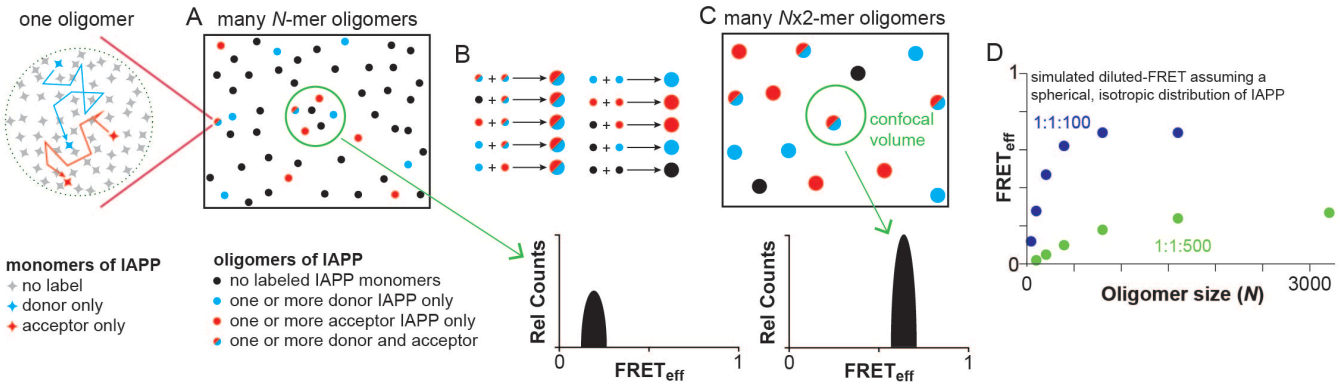

Figure 7: A model for oligomer growth

(A) Two-dimensional representation of many IAPP oligomers of size *N*. At high label dilution, most oligomers do not include a fluorophore labeled IAPP. The confocal imaging volume is represented as a green circle with the time averaged $FRET_{eff}$ distribution shown schematically. Left, a hypothetical single oligomer containing many unlabeled IAPP and a single donor and a single acceptor labeled IAPP. Observation of a narrow $FRET_{eff}$ can be reconciled by random-walk (shown as colored arrows) motion of IAPP within the oligomer.

(B) Oligomers present in (A) merge to form larger oligomers. All combinatorial possibilities are shown. (C) IAPP oligomers of size *2N*. Fewer oligomers are now label-free resulting in higher apparent $FRET_{eff}$ and higher apparent counts.

(D) Simulated average $FRET_{eff}$ for a dynamic, isotropic spherical distribution of an IAPP oligomer of size *N*. Each IAPP molecule is assumed to occupy 4000 $Å^3$, a Förster distance of 52 Å, the indicated ratio of (donor labeled IAPP):(acceptor labeled IAPP):(unlabeled IAPP), and the indicated oligomer size.